



## Research Article

# Design and development of a high-performance Ni-based superalloy WSU 150 for additive manufacturing



Praveen Sreeramagiri, Ajay Bhagavatam, Abhishek Ramakrishnan, Husam Alrehaili, Guru Prasad Dinda \*

Department of Mechanical Engineering, Wayne State University, Detroit, MI, 48202, USA

## ARTICLE INFO

### Article history:

Received 11 October 2019

Received in revised form

19 December 2019

Accepted 7 January 2020

Available online 21 February 2020

### Keywords:

Ni-based superalloys

Additive manufacturing

Laser metal deposition

Ripple pattern microstructure

Alloy development

Mechanical properties

## ABSTRACT

This research proposes a design and development strategy of a new nickel-based superalloy for additive manufacturing. A new Ni-based superalloy has been developed by the application of the combinatorial alloy development technique coupled with CALPHAD based solidification modeling by effectively suppressing the precipitation kinetics. The suppression of precipitation during processing paved a way for prevention of cracks during deposition. The new alloy "WSU 150" revealed excellent room temperature mechanical properties with a yield strength of 867 MPa, an ultimate tensile strength of 1188 MPa, and an elongation of 27.9% in the as-deposited condition. The mechanical properties of the heat-treated alloy were improved significantly to 1114 MPa yield strength, 1396 MPa ultimate tensile strength, and an elongation of 16.1%. Improvement in the mechanical properties is attributed to the additional precipitation and coarsening of  $\gamma'$  and carbides during heat-treatment. Microstructural investigation of the alloy revealed spherical  $\gamma'$  with a rippled size distribution from the center to the interdendritic region. The average size of the  $\gamma'$  particles in the as-deposited condition was found to be around 48 nm in the interdendritic region. Heat-treatment promoted the coarsening of  $\gamma'$  which is explained in the paper.

© 2020 Published by Elsevier Ltd on behalf of The editorial office of Journal of Materials Science & Technology.

## 1. Introduction

Additive manufacturing (AM) is an emerging technology in the field of manufacturing. It is one of the most versatile processes which can produce near net-shaped products. This process creates a physical component by layering the material in accordance with the digital (CAD) model. It eliminates the utilization of tools, dyes, punches, etc., which reduce prototyping costs. Based on the existing AM techniques, several machines are available in the market to print a variety of materials like polymers, plastics, composites, metals, etc. [1–3]. This research emphasizes on Laser metal deposition (LMD), an additive manufacturing process, which can print components with a variety of metals. It utilizes laser power to melt a feed material (typically metal powder or wire) and fuse the material in the above-mentioned fashion to produce the components from a CAD model. This process is categorized under 'directed energy deposition' (DED) as the energy is being directed at a point to pro-

cess the metal. This process has the potential to produce complex geometries, which are hard to be processed by conventional manufacturing techniques and repair broken or worn-out components. The aforementioned reasons constitute for additive manufacturing to be one of the most interesting topics of research in academia and industry. The LMD is unique with characteristics such as high cooling rate (typically of the order of  $10^3$  or  $10^5$  K/s), rapid solidification, etc. [4]. These characteristics can be used in tailoring the microstructure of the material that affects the mechanical properties significantly. While these characteristics can help to process the material in multiple ways, some problems such as hot tearing, heat affected zone (HAZ) cracking, etc. [5], associated with compositional segregation, can be the consequences of the process.

Nickel-based superalloys assert a very good application in gas turbine blades and nuclear applications [6–8]. Primarily nickel exhibits a face-centered cubic (FCC) structure ( $\gamma$ ) and it is alloyed to improve the mechanical properties by different mechanisms, and these are termed Ni-based superalloys. One of such strengthened mechanisms is precipitation strengthening. The precipitation in these alloys is caused by two different precipitates. One of which is the ordered L12 FCC  $\gamma'$  ( $Ni_3(Al, Ti)$ ) phase and the other is a body-centered tetragonal  $\gamma''$  ( $Ni_3Nb$ ). Several commercially

\* Corresponding author at: Wayne State University, 5050 Anthony Wayne Dr, Detroit, MI, 48202, USA.

E-mail address: [dinda@wayne.edu](mailto:dinda@wayne.edu) (G.P. Dinda).

available Ni-based superalloys were developed for conventional manufacturing processes such as casting, forging, etc. Comprehensive experiments have been performed across the globe to test the compatibility of these available precipitation-strengthened superalloys for AM [2,4,5,9–12]. However, several studies reveal the non-compatibility of these available Ni-based superalloys (containing more than 50% volume fraction  $\gamma'$  particles) for AM, due to the above-mentioned reasons (solidification and liquation cracking, etc. [9–12], by the supersaturation of the composition and strengthening phases of  $\gamma'$ ). Processing of nickel-based superalloys through AM receives attention in the aerospace, nuclear and other industries. This opens a new horizon for research towards the development of new novel high-performance alloys that can be successfully processed by additive manufacturing. The unique processing methodology of LMD can be accounted for in favor of the new alloy development by in-situ composition optimization. This enhances the researcher, to easily customize the chemical composition of the alloy while processing the material to obtain knowledge on the possible phases of any complex material system.

The necessity to fabricate high strength Ni-based superalloys through AM thrusts the development process of new Ni-based superalloys. This constitutes the main objective of the current research. This work presents the development of a novel Ni-based superalloy WSU 150 for AM, by the application of combinatorial/high-throughput alloy development technique [13–19] coupled with CALPHAD based solidification modeling [20–22]. The new alloy revealed defect-free depositions with excellent mechanical properties.

## 2. Experimental procedure

### 2.1. Equipment

Laser metal deposition (LMD) equipment developed at Wayne State University has been utilized for the new alloy development. The equipment consists of an ABB 6-axis robot (IRB 1410) to which a 2KW diode laser (Laserline LDM 2000-1000) is connected and the laser beam is directed through a co-axial nozzle. The design of the nozzle facilitates the powder stream to converge at the focal point of the laser beam. This enables the laser to melt the substrate and powder when converged at the same point. The powder is supplied through a Bay State 1200SP-1 Powder Feeder. The laser beam moves with the robot which is directed as per the path generated by the slicing software for a CAD model. The movement of the laser beam along with the feed material generates a clad of material, and cladding, when performed as per the geometry, produces the required part. The equipment employed in the LMD at Wayne State University is presented in Fig. 1.

### 2.2. Material and methods

Gas atomized powder with a mesh size ranging from –100 to +325 obtained from Carpenter Powder Products was utilized to process the deposits. The design of a Ni-based superalloy for AM can be a challenging issue. Combinatorial/high-throughput alloy development technique signifies one of the versatile methods to develop a new alloy and has been reported by many researchers for new alloy development [14]. A combinatorial alloy development technique utilizes two or more existing alloys or elements that can be mixed, to analyze the micro-constituents of a variety of compositions. Diverse elements/alloy systems can be mixed in a variety of proportions. Each of the different proportions developed is a new composition and ultimately a material. By direct laser metal deposition, multi-component materials can be synthesized by fusion of the incoming powders followed by in-situ mixing of

the different powders, which can be applied for the combinatorial alloy development technique with ease. The in-situ composition change can assist with the processing of various proportions of different elemental/alloy systems by utilizing the gradient approach. When a gradient sample is processed by AM, each pixel of the deposit exhibits a different composition, which can be explored. The process is explained in detail as follows.

Two powder feeders (hoppers), each containing different alloys were employed, and a gradient composition has been programmed. For the current investigation, the alloys utilized were, an alloy which is categorized under low  $\gamma'$  volume fraction alloy (alloy A) and an alloy which can be classified as a high  $\gamma'$  volume fraction alloy (alloy B). The gradient deposit contains 100% of alloy A on one end of the sample and it steadily decreases (1% change for every bead in the current case) while the alloy B quantity is increased corresponding to the decrease of the first alloy quantity. To formulate this practically, the voltage of the motor was operated as a function of flow rate. Therefore, the variation of the voltage supplied to the hopper provides a gradient sample, which is represented in Fig. 1(b). The gradient composition for this study was programmed on the XY-plane (i.e., from left to right), which ensures the Z-direction which is the build direction (bottom to top), to follow the composition from the previous layer at the corresponding locations. The gradient sample obtained from the two alloys was visually inspected followed by microstructural investigation to analyze the defects (such as cracks) in the deposit. Microscopic images in distinct zones of the gradient sample are presented in Fig. 2. The volume fraction of  $\gamma'$  particles is observed to increase from alloy A to alloy B as a result of varying composition. It should be emphasized that the as-deposited sample corresponding to the images of Fig. 2(a) through Fig. 2(d) are friendly for laser deposition and showed no relevant process defects such as cracks and porosity. In contrast, high  $\gamma'$  volume fraction composition corresponding to Fig. 2(e) through Fig. 2(h) revealed the presence of cracks in the as-deposited samples. Further, the gradient sample has been evaluated for hardness at various zones on the XY plane (cut in Z-section) at regular intervals (intervals at 5% compositional change). This investigation reports the detailed microstructural evolution and mechanical response of an alloy WSU 150 corresponding to Fig. 2(c) which revealed an optimum hardness of 375 HV (at one location in the gradient composition) with no relevant defects. The composition of WSU 150 alloy, which is at the zone of Fig. 2(c) in the gradient sample was evaluated by the application of energy dispersive X-Ray spectroscopy (EDS) and is listed in Table 1. Initially, the design of experiments was conducted on the composition (WSU 150) to achieve a near 100% density. Further, a block was processed for the tension test samples which is discussed in detail in the following sections.

### 2.3. Design of experiments

A design of experiments (DOE) technique was conducted on the WSU 150 alloy to obtain the optimum process parameters that ensure a near 100% density. Process parameters such as travel speed, laser power, and powder flow rate play a vital role to produce relevant defect-free (near 100% density and optimum strength) deposits. For instance, a high powder feed and travel speed with a lower power is not adequate to melt all the metal being supplied. Therefore, the determination of the optimum process parameter window is crucial for the LMD process. In the current investigation, the design of experiments (DOE) was conducted based on a well-known principle of the Taguchi L9 matrix. The optimized process parameters utilized for the deposition of the alloy are listed in Table 2. These parameters result in near 100% density of the component with a sound metallurgical bond.

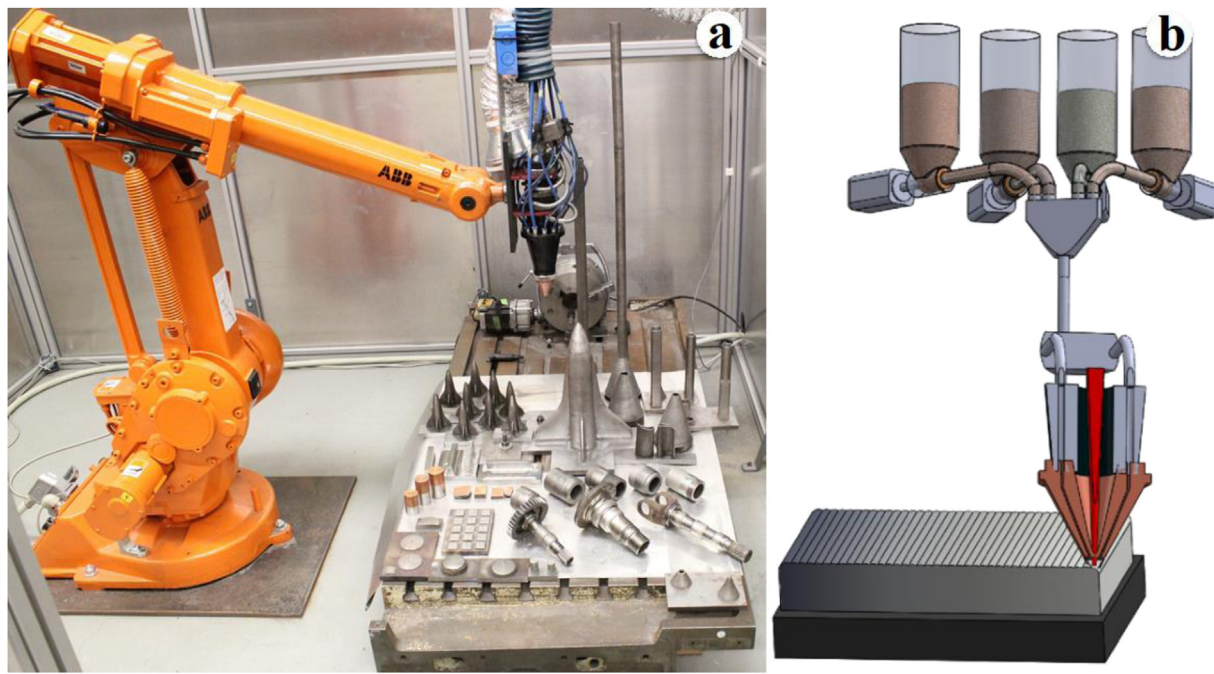


**Fig. 1.** Robotic laser metal deposition (LMD) equipment developed at Wayne State University. (a) Robotic arm with a nozzle attached through the optical fiber, (b) Image demonstrating the combinatorial alloy development technique with LMD.

**Table 1**  
Chemical composition of the new WSU 150 alloy powder.

Element (Wt%)	Ni	Cr	C	Mo	Co	W	Cb (Nb)	Ti	Ta	Al
WSU150	59.64	17.83	0.09	5.3	9.29	1.33	0.45	2.75	0.9	2.44

**Table 2**  
Process parameters used for the deposition of WSU 150.

Alloy	Laser Power (Watt)	Scan Speed (mm/min)	Powder Flow Rate (gm/min)	Shaping Gas (ft <sup>3</sup> /hr)	Powder Carrier Gas (ft <sup>3</sup> /hr)
WSU 150	750	720	14.5	15	15

#### 2.4. Thermodynamic simulation

In order to understand and characterize the phases in the alloy system, this composition was analyzed using thermodynamic simulation with the CALculation of PHase Diagram (CALPHAD) technique. The simulation was performed using the Thermo-Calc TCNI8 thermodynamic database to estimate the amount of  $\gamma'$  phase that can be formed with the proposed chemical composition.

#### 2.5. Mechanical testing and microstructural investigation

A detailed study has been conducted to analyze the mechanical properties and microstructure of WSU 150 in the as-deposited and heat-treated conditions. A block shown in Fig. 3(a) was deposited with the composition listed in Table 1 for the preparation of the tension test samples. The block was further cut to multiple test samples by the application of EDM to the dimensions as shown in Fig. 3(b). The tool path for the block consisted of a cross-hatch pattern to ensure near isotropic material properties. For the microstructural investigation, cylindrical samples have been processed. A detailed microstructural investigation was performed on the samples both in as-deposited and heat-treated conditions. The design of heat-treatments was based on the factors that contribute

to the formation of  $\gamma'$  (primarily aluminum and titanium in this case) and the precipitation of carbides. The concentration of the aluminum and titanium (wt.%) in this alloy were considered to select an appropriate heat-treatment temperature. The weight percent was compared to several existing alloys and the heat-treatment for alloys such as M22, Rene 88DT [23], etc., was utilized. Heat-treatment of the sample was performed at 760 °C for 4 h in an MTI OTF-1200X tube furnace. The samples were mounted, polished and etched in 12 ml H<sub>3</sub>PO<sub>4</sub> + 40 ml HNO<sub>3</sub> + 48 ml H<sub>2</sub>SO<sub>4</sub> at 6 V for 8 – 10 s to investigate the microstructure. The etching was performed to reveal the  $\gamma'$  phase. High-resolution microstructural imaging was performed using the scanning electron microscope (JOEL-7600 FE SEM) and compositional analysis was performed using energy dispersive X-Ray spectroscopy (EDAX Pegasus Apex 2). The X-Ray Diffraction analysis (XRD) has been performed on the sample in Bruker X8 DaVinci A25 Powder Diffractometer with a Cu K<sub>α</sub> radiation ( $\lambda = 1.5418 \text{ \AA}$ ). The investigation was performed for standard  $\theta - 2\theta$  geometry with the angle varying from 20°–100°.

The mechanical properties (tensile) of the samples were evaluated using the Universal Tensile Testing Machine (MTS 810) on the coupons shown in Fig. 3(c). All the tests were performed at room temperature. Load measurement was carried out with a load cell of sampling rate 1000 Hz and strain measurement with a strain rate of 0.2 mm/min.

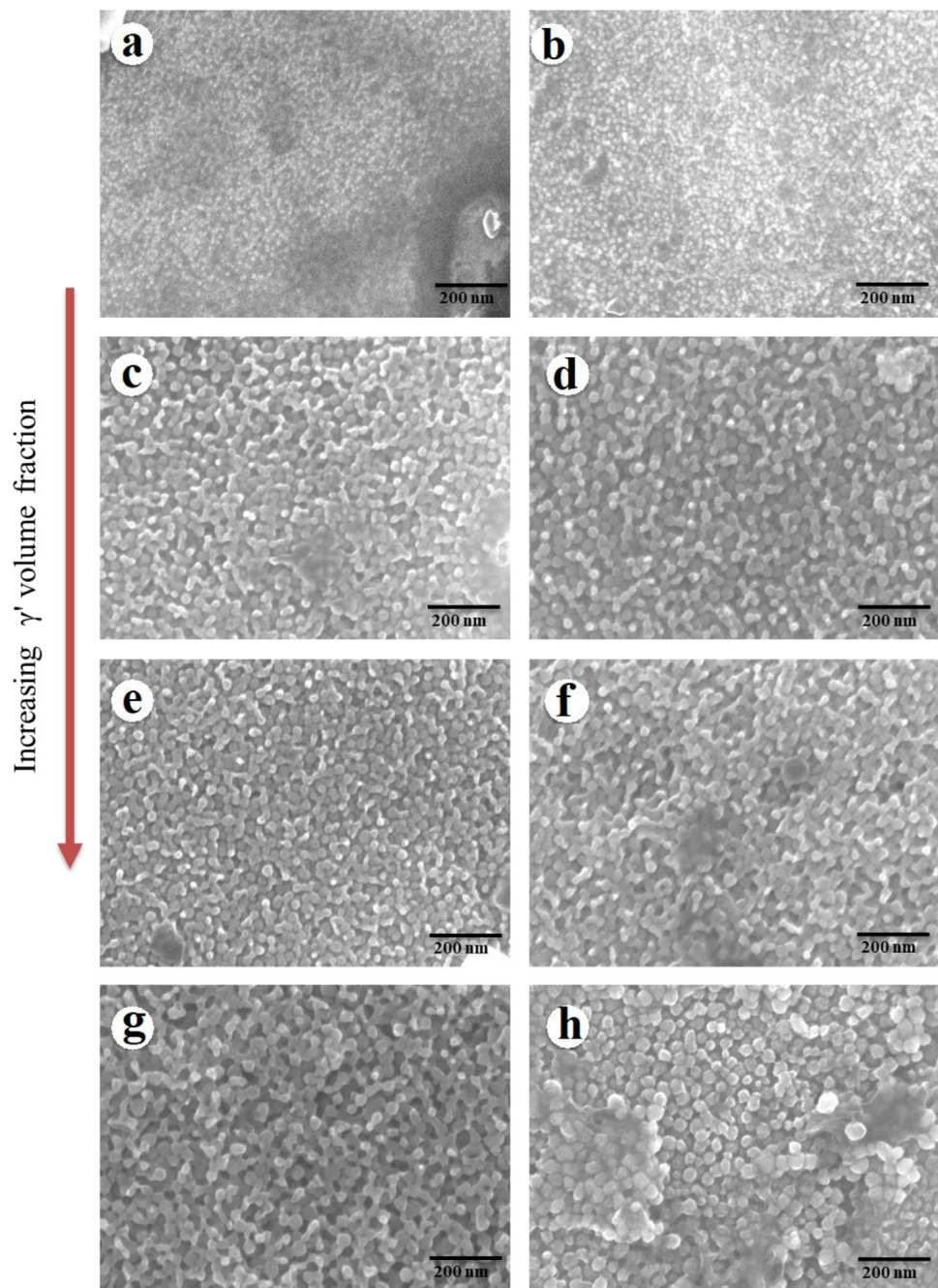


**Fig. 2.** SEM images of the as-deposited gradient samples showing the microstructural morphology of  $\gamma'$  particles. (a → h) Showing the increasing trend of size and volume fraction of  $\gamma'$  with the increase of high  $\gamma'$  alloy content in the sample.

### 3. Results and discussion

#### 3.1. CALPHAD simulation

The numerical analysis provides information on the potential phases that an alloy can exhibit. The equilibrium solidification model based on Thermo-Calc TCNi8 thermodynamic database was employed to simulate composition and volume fraction of equilibrium phases in the multicomponent Ni-alloy system. The phase distribution and the elemental segregation as per the composition have been calculated and the results are presented in Fig. 4. The equilibrium simulation predicts 38% volume fraction of  $\gamma'$  precipitates which is represented in Fig. 4(a). The solvus temperature of the

$\gamma'$  was found to be 1050.7 °C. The extent of micro-segregation due to the rapid solidification during AM was assessed by the Scheil-Gulliver model, which is presented in Fig. 4(b). According to this, it can be observed that nickel being the primary element is evenly distributed till the end of the solidification and is reduced at the end. Chromium, cobalt, molybdenum, etc., which form an excellent solid solution with the Ni matrix have a similar distribution pattern to that of Ni. Elements like tantalum, tungsten, etc., which form the refractory element group are partially rejected by the matrix and are segregated to the later part of the solidification which is the interdendritic region. This can be observed from the lines in Fig. 4(b) that ascend as it proceeds to the mole fraction 1. The principal  $\gamma'$  forming element Al is well distributed in the matrix

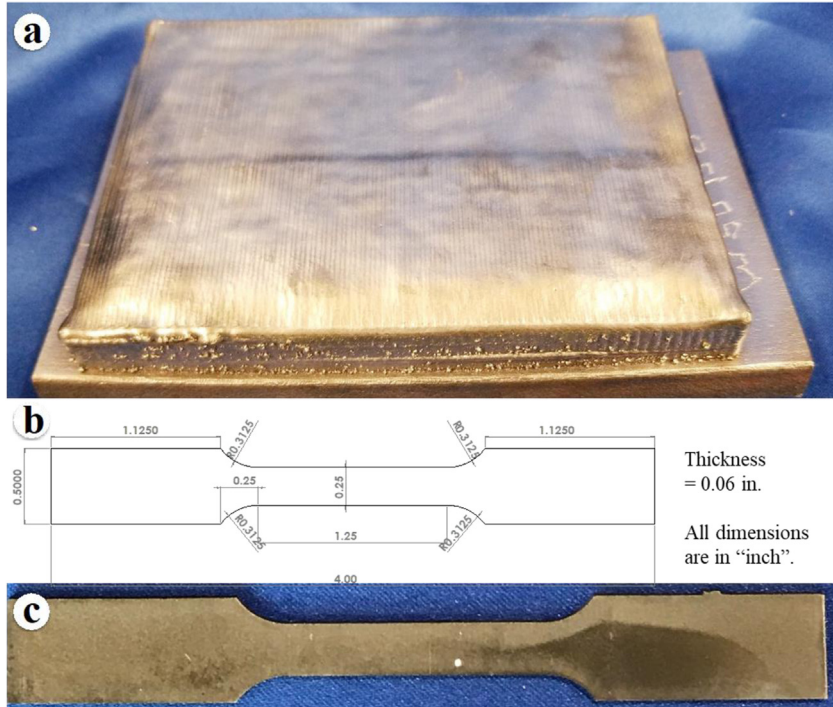


**Fig. 3.** (a) Block deposited for the tension test coupons, (b) Tension test sample dimensions in accordance with ASTM E8 standards, (c) Tension test sample prepared according to (b).

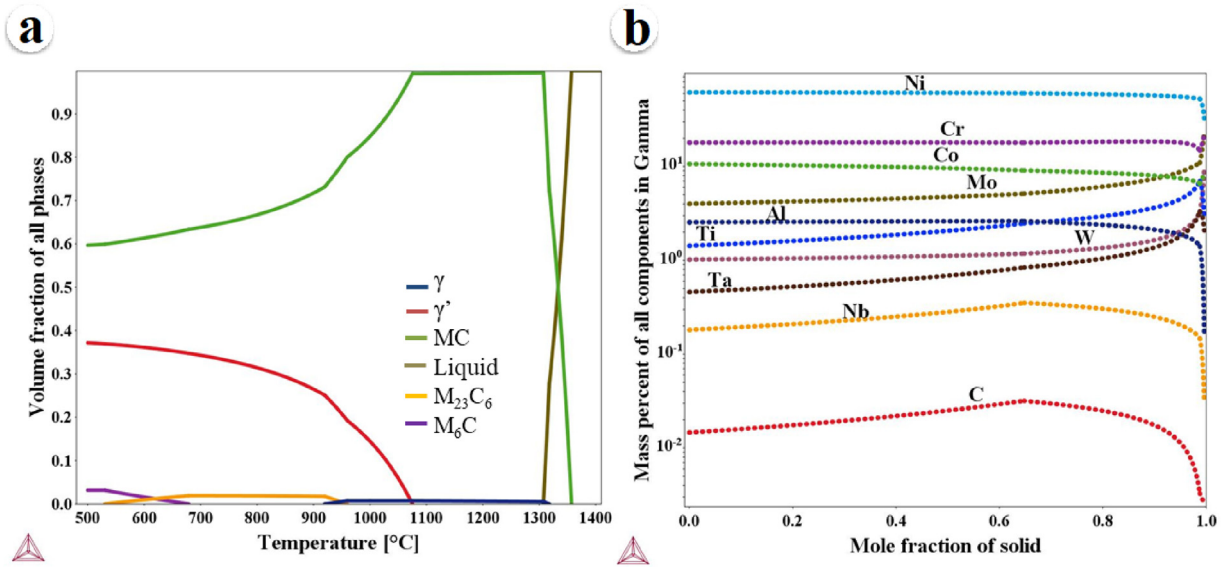


**Fig. 4.** (a) CALPHAD based solidification modeling for WSU 150, (b) Schiel based elemental segregation model for WSU 150 from start to the end of solidification.

during solidification. While another  $\gamma'$  forming element, which is Ti, is partly rejected to the interdendritic region, which is the final zone of solidification. The carbon which is another important element is observed to increase as it goes to the end and decreases as the solidification ends. This has a major influence on the carbides that can be observed in the alloy. These segregation patterns are attributed to the affinity of the element towards the  $\gamma$ -Ni matrix. These analyses were performed with the assumption that the element has infinite diffusivity in liquid-state but zero diffusivity in the solid-state. However, for a rapid cooling process such as LMD, these tools may not be 100% assertive. Nevertheless, these can be verified to an extent practically with the application of the EDS analysis which is reported in later sections.

### 3.2. Microstructural investigation

A detailed microstructural investigation has been performed on the newly developed alloy both in the as-deposited and post-heat-treated conditions. The microstructure of the as-deposited condition is presented in Fig. 5. The as-deposited sample exhibited a dendritic morphology, which can be observed in Fig. 5(a). As a result of rapid cooling, coring was observed from the center to the interdendritic region. This, as explained earlier, is the phenomenon of elemental rejection by the matrix phase and compositional segregation during solidification. The sample contains well-defined near-spherical  $\gamma'$  particles all over the area. The size of the  $\gamma'$  averaged to about 25.6 nm in the center core. The  $\gamma'$  particle size has

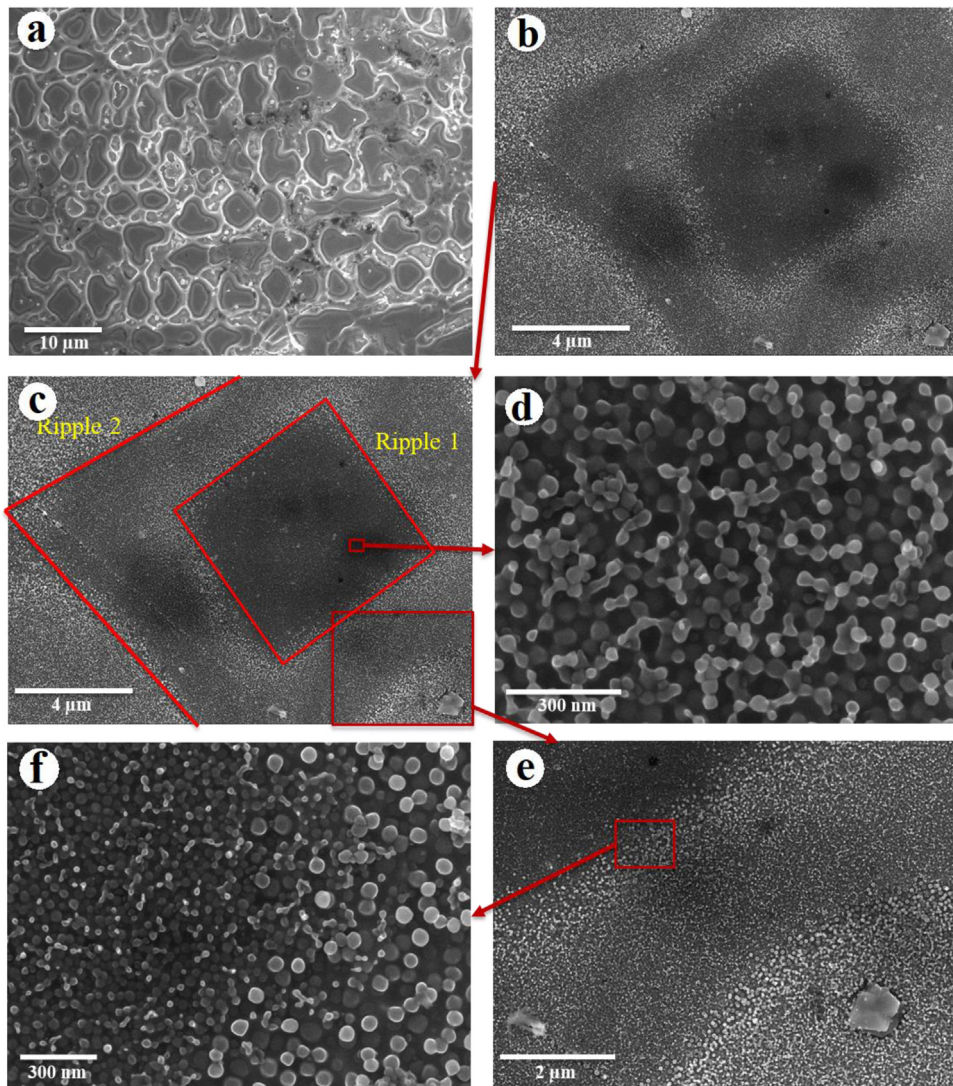


**Fig. 5.** SEM analysis of as-deposited WSU 150. (a) Low magnification image showing the dendrite (gray contrast) and interdendritic region (lighter region), (b-c) Dendrite with different cores, (d)  $\gamma'$  particles at the center of the dendrite, (e) Transition zone of two cores with a different precipitate size distribution, and (f) Magnified view of (c) showing different cores and size distribution of  $\gamma'$  particles.

been observed to increase as it proceeds away from the center. However, an intriguing size distribution has been observed from the dendrite core to the interdendritic region, which consisted of two distinct ripples. The size of the  $\gamma'$  particles in these two ripples followed a different trend. These ripples possess a slightly increased  $\gamma'$  size, which is deviated from the actual size distribution. As the ripple is crossed, the size of the  $\gamma'$  reduces to the sequential growth from the previous core. This was found to be the result of compositional variation at these locations by a definite set of elements like Ta, which was evident from the EDS analysis. This is discussed in the later sections. The variation in the size was observed until the end of the solidification, which is the interdendritic region. The size of the  $\gamma'$  particles averaged to about 48 nm in the interdendritic region. Measurements for the  $\gamma'$  precipitate size have been performed on over 5 SEM images from the sample over different magnifications such as 50,000x, 75,000x, etc.

The sample has been aged at 760 °C for 4 h. A similar microstructural investigation has been carried out on the heat-treated sample. Since the sample was subjected to aging alone, no homogenization of the composition has been observed and the dendritic morphology and the ripple effect persists. However, there might be slight solid-state diffusion of some elements possible during this

period. Coarsening of the  $\gamma'$  precipitates has been observed near the interdendritic regions and the size averaged to be 53 nm after heat-treatment. The dendrite core areas are now decorated with continuous and attached (about to merge) near-spherical  $\gamma'$  particles. The interdendritic regions and grain boundaries are now decorated with carbide particles of various shapes, as shown in Fig. 6(b). A significant increase in the volume fraction of carbides was observed after the heat-treatment. In Ni-based superalloys, from 750 °C – 1000 °C the MC (M-Ti, Mo) decompose form  $\gamma'$  and  $M_{23}C_6$  (M-Cr, Mo) carbides. The precipitation of these carbides also contributes to the increase in strength after heat-treatment.

The composition of the sample has been analyzed by the application of EDS and the results are presented in Fig. 7. Different ripples in the dendritic region have been investigated to explain the possibilities of variation in the size of  $\gamma'$  particles. The dendrite core area is presented in Fig. 7(a) and the core to the interdendritic area is reported in Fig. 7(b). The EDS analysis confirms the elemental composition with no loss of elements in the alloy during deposition. Majority of the elemental segregation concord the simulation results. However, it can be noticed in Fig. 7(b) that the segregation of some elements like aluminum, tantalum, etc., contradicts the simulation and exhibit a different pattern. The concentration of

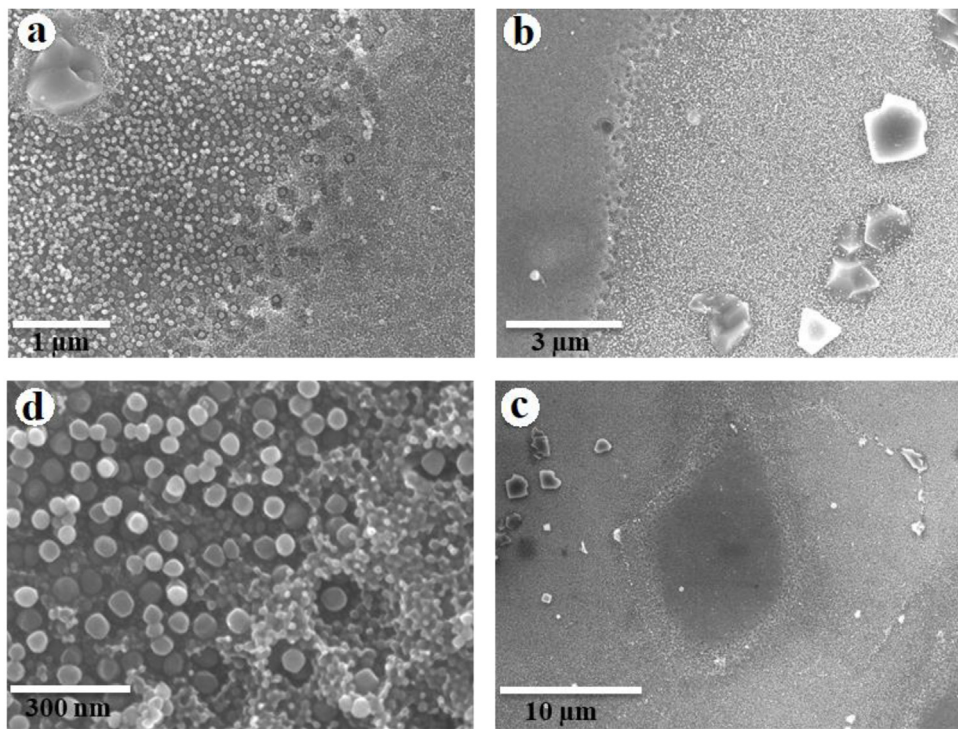


**Fig. 6.** SEM analysis of WSU 150 aged at 760 °C for 4 h, (a) Transition from one core to other core, (b) Dendrite and interdendritic region with carbides in the interdendritic region, (c) Dendrite and interdendritic region, (d) Magnified view of (a) showing different cores and size distribution of  $\gamma'$  particles.

aluminum increased from the center of the dendrite to the interdendritic region. This can be attributed to the comparatively low affinity of the element towards the matrix phase and the high diffusivity of Al. The concentration of Ta was found to be fluctuating from center to the interdendritic region. This promoted a variation in the size of  $\gamma'$  particles from the dendrite core to the interdendritic region. An increased concentration of Ta contributed to finer  $\gamma'$  precipitates, while decreased concentration promoted coarser  $\gamma'$  precipitates. This is related to the precipitation and coarsening kinetics of  $\gamma'$  when Ta is under consideration. Ta is a heavier element and it relatively reduces the coarsening kinetics compared to the other  $\gamma'$  forming elements like Al and Ti. However, the reason for the fluctuation of Ta concentration is still to be understood. Nevertheless, LMD being a rapid cooling process, a very complex thermal history is experienced by each pixel in the sample. Every point in the deposition experiences multiple heating and cooling cycles. This complex heating and cooling cycles along with the compositional influence is believed to have a strong effect on the segregation (in liquid state) and diffusion (both in liquid and solid-state) of elements like Ta, which is the primary element responsible for the shift in the size of  $\gamma'$  particle in the ripple zone. Other  $\gamma'$  forming elements like Al and Ti have a definite pattern of segregation during solidification which is evident from the EDS in Fig. 7(b) and these elements have the least effect on the ripple pattern of  $\gamma'$  size (See Table 3).

### 3.3. X-ray diffraction

The X-Ray diffraction (XRD) analysis was performed on the alloy both in as-deposited and heat-treated conditions. The results are presented in Fig. 8. Various peaks of different planes of  $\gamma$ ,  $\gamma'$ , MC and  $M_{23}C_6$  carbide phases can be observed from the results. The lattice parameter of  $\gamma/\gamma'$  was found to be 358.8 pm in the as-deposited condition and 358.7 pm in the heat-treated condition. A slight mismatch is observed after the heat-treatment which is the result of compositional diffusion during heat-treatment. The carbide peaks

**Table 3**  
The EDS analysis on the sample referenced to Fig. 7.

(a)		1 Wt.%	2 Wt.%	3 Wt.%
Location	Element			
Al		19.59	2.81	2.73
Ta		1.32	1.84	1.72
W		2.98	2.5	2.79
Mo		5.26	5.28	5.31
Ti		2.02	2.32	2.29
Cr		14.83	17.6	17.64
Co		7.87	9.46	9.91
Ni		46.13	58.18	57.62

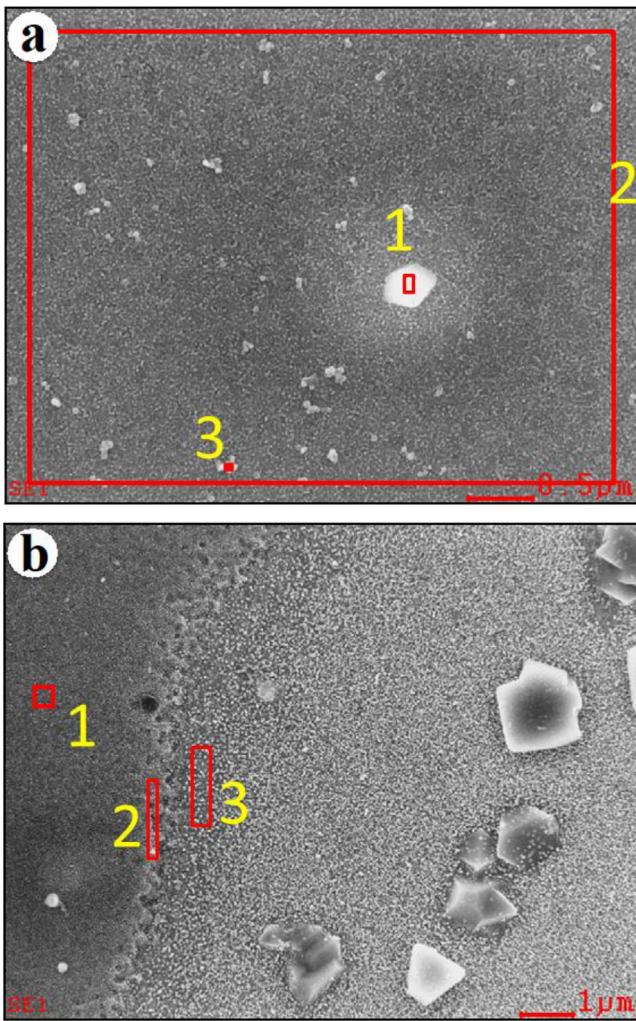
  

(b)		1 Wt.%	2 Wt.%	3 Wt.%
Location	Element			
Al		2.84	2.83	2.91
Ta		1.91	1.83	1.98
W		2.37	2.73	2.53
Mo		5.02	5.21	5.43
Ti		2.38	2.56	2.79
Cr		17.75	17.81	17.5
Co		9.24	9.03	8.97
Ni		58.5	58.01	57.9

of MC and  $M_{23}C_6$  observed are very weak since the volume fraction of the carbides is very low in the alloy. However, a slight increase in the carbides peak reveals the increased volume fraction after heat-treatment.

### 3.4. Mechanical properties

The tension test was performed on the samples shown in Fig. 3 using the MTI universal testing machine. A load measurement was performed using the load cell in the machine. Strain measurement was performed using an extensometer of 25 mm gauge length. The results from the tension test were found and are sum-



**Fig. 7.** (a-b) Locations of EDS analysis performed on the WSU 150 alloy.

marized in **Table 4**. The test was performed on three samples in each of the specified conditions and the results were averaged. The tests revealed a yield strength of 866 MPa and an ultimate tensile strength of 1187 MPa with an elongation of 27.9% in the

**Table 4**  
Mechanical properties of the as-deposited and the heat-treated WSU 150.

Condition Name	Units	AD WSU150	HT @760 °C/4 h
Young's Modulus 'E'	GPa	191.32	201.84
Yield Strength	MPa	867	1113.84
Ultimate Tensile Strength 'UTS'	MPa	1188	1396
Engineering Strain at UTS	%	27.57	16.05
% Elongation	%	27.9	16.1
Fracture Stress	MPa	1164.04	1386.32

as-deposited condition. Tensile test plots of the material in the as-deposited and different heat-treated conditions are presented in **Fig. 9(a)**. A bar graph representing the mechanical properties of various heat-treated alloys has been presented in **Fig. 9(b)**. Of all the tests performed, the sample which was heat-treated at 760 °C for 4 h revealed a very good combination of ultimate tensile strength, which was found to be 1396 MPa, yield strength of 1114 MPa, and ductility of 16.1%. These results were found to be very promising in comparison with the existing commercial alloys like Haynes 282, which can be processed by additive manufacturing. Alloys like René 88DT which exhibit a similar  $\gamma'$  volume fraction were not explored with AM process to our best knowledge. However, properties of WSU 150 are superior to heat-treated René 88DT produced through the powder process. The properties of René 88DT as reported in the ASM handbook [24] were found to be 1143 MPa with an elongation of 20%.

It is evident from the results that heat treatment significantly increased the strength of the material. The increase in strength is believed to be the consequence of the various factors during heat-treatment such as additional precipitation and coarsening of  $\gamma'$  precipitates (significantly in the dendrite core region), precipitation and coarsening of carbides, etc. The  $\gamma'$  particles as stated above are attached to each other. This signifies the particles are about to merge and coarsen, which signifies increased volume fraction and reduced distance between particles. As the distance between particles decreases, the force required for the dislocation motion to cut the  $\gamma'$  particle at the onset of yield increases. This is applicable when the precipitates ( $\gamma'$ ) are coherent with the matrix. The mechanical properties of the alloy are assumed to be isotropic, as a cross-hatch pattern was employed in the deposition. However, it is to be validated by testing the sample in different orientations of the deposit.

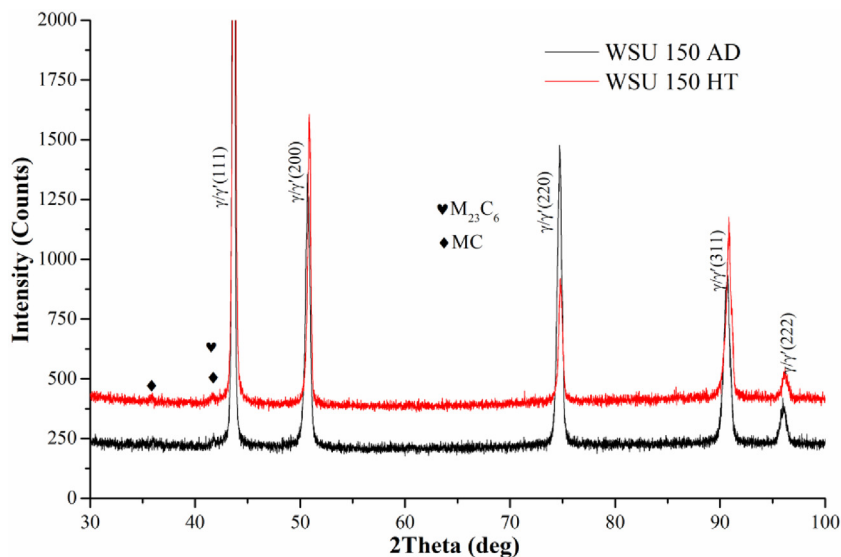


**Fig. 8.** X-ray diffraction pattern of the as-deposited and heat-treated WSU 150 samples.

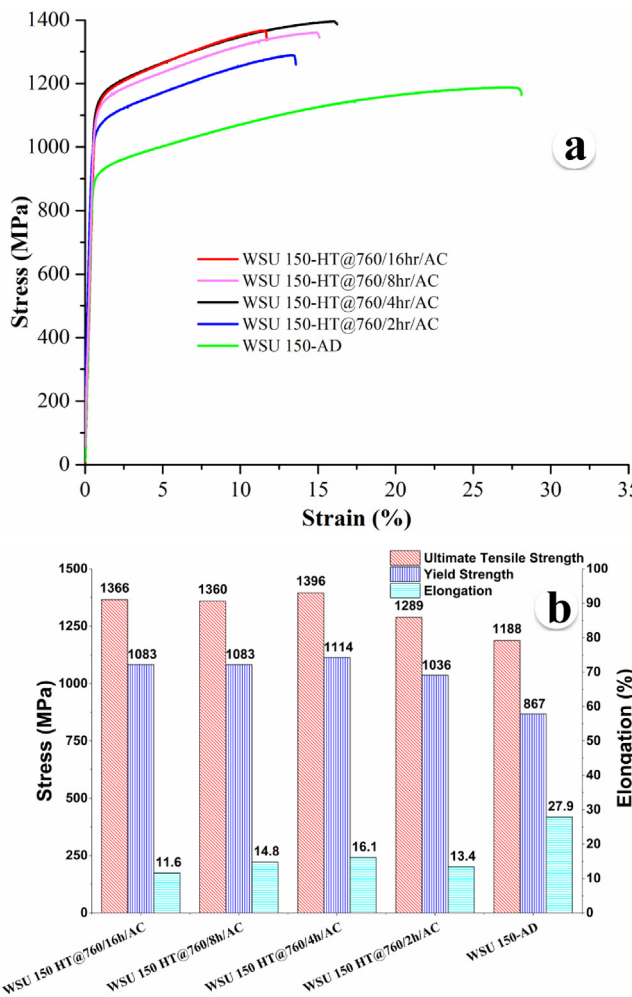


**Fig. 9.** (a) Tension test results of WSU 150 conducted in as-deposited and different heat-treated conditions, (b) Bar chart representing strength and ductility of various as-deposited and heat-treated conditions.

#### 4. Conclusion

A novel Ni-based superalloy has been developed specifically for additive manufacturing which can be used for various high-temperature applications around 800 °C. Techniques such as combinatorial alloy development and CALPHAD based solidification modeling were utilized for this purpose. The newly developed alloy revealed a  $\gamma'$  volume fraction of about 38%. A detailed microstructural investigation on the sample revealed the  $\gamma'$  size to be around 48 nm in the as-deposited condition and around 53 nm in the heat-treated condition. A ripple pattern in the  $\gamma'$  size distribution has been observed which is caused by the segregation of 'Ta'

in the alloy system. However, further investigation is required to study the segregation behavior of Ta. The alloy revealed excellent room temperature mechanical properties with a yield strength of 867 MPa, an ultimate tensile strength of 1188 MPa and a ductility of 27.9 in the as-deposited condition. Heat-treatment performed on the sample had a significant effect on the mechanical properties increasing the yield strength to 1114 MPa, UTS to 1396 MPa, and the elongation has been reduced to 16.1%. Additional precipitation and coarsening of  $\gamma'$ , carbides and increased coherency of precipitates were found to be the causes of increased strength post-heat-treatment. Further tests must be conducted to investigate the high-temperature mechanical properties.

#### Data availability

Data will be made available on request.

#### Acknowledgment

The authors gratefully acknowledge the financial support from the U.S. Department of Energy and Advanced Powder Solutions (DE-SC0015743).

#### References

- [1] N. Li, S. Huang, G. Zhang, R. Qin, W. Liu, H. Xiong, G. Shi, J. Blackburn, J. Mater. Sci. Technol. 35 (2) (2019) 242–269.
- [2] G.P. Dinda, Mater. Sci. Eng. A Struct. Mater. 509 (1-2) (2020) 98–104.
- [3] A. Bandyopadhyay, B. Heer, Mater. Sci. Eng. R Rep. 129 (2018) 1–16.
- [4] M.M. Attallah, R. Jennings, X.Q. Wang, L.N. Carter, MRS Bull. 41 (10) (2016) 758–764.
- [5] D. Tomus, P.A. Rometsch, M. Heilmayer, X.H. Wu, Addit. Manuf. 16 (2017) 65–72.
- [6] T.M. Pollock, S. Tin, J. Propuls. Power 22 (2) (2006) 361–374.
- [7] N. R. Mukutnatapalati, 2011.
- [8] C.A.E.M. Scientia et Technica Año (2020).
- [9] E. Chauvet, P. Kontis, E.A. Jagle, B. Gault, D. Raabe, C. Tassin, J.J. Blandin, R. Dendievel, B. Vayre, S. Abed, G. Martin, Acta Mater. 142 (2018) 82–94.
- [10] M. Cloots, P.J. Uggowitzer, K. Wegener, Mater. Des. 89 (2016) 770–784.
- [11] H. Peng, Y. Shi, S. Gong, H. Guo, B. Chen, Mater. Des. 159 (2018) 155–169.
- [12] A. Ramakrishnan, G.P. Dinda, Mater. Sci. Eng. A 740–741 (2019) 1–13.
- [13] M.M. Khan, I. Shabib, W. Haider, Scr. Mater. 162 (2019) 223–229.
- [14] A. Deschamps, F. Tancre, I.-E. Benrabah, F. De Geuser, H.P. Van Landeghem, C. R. Phys. 19 (8) (2018) 737–754.
- [15] A. Kauffmann, M. Stuber, H. Leiste, S. Ulrich, S. Schlabach, D.V. Szabo, S. Seils, B. Gorr, H. Chen, H.J. Seifert, M. Heilmayer, Surf Coat Tech 325 (2017) 174–180.
- [16] R. Ölmez, G. Çakmak, T. Öztürk, Int. J. Hydrogen Energy 35 (21) (2010) 11957–11965.
- [17] M. Polanski, M. Kwiatkowska, I. Kunce, J. Bystrzycki, Int. J. Hydrogen Energy 38 (27) (2013) 12159–12171.
- [18] R. Vilar, R. Colaço, Surf. Coat. Technol. 203 (19) (2009) 2878–2885.
- [19] X. Zhang, Y. Xiang, J. Mater. 3 (3) (2017) 209–220.
- [20] C.-W. Li, K.-C. Chang, A.-C. Yeh, J.-W. Yeh, S.-J. Lin, Int. J. Refract. Metals Hard Mater. 75 (2018) 225–233.
- [21] S. Meher, M.C. Carroll, T.M. Pollock, L.J. Carroll, Mater. Des. 140 (2018) 249–256.
- [22] H. Lukas, 'Computational Thermodynamics : the CALPHAD Method', Cambridge University Press, 2007.
- [23] S. Włodek, M. Kelly, and D. Alden.
- [24] H. J. C. Ahluwalia, 2002, 58(4), 381.